

Deep Sea Bubble Stream Characterization Using Wide-Baseline Stereo Photogrammetry

Mengkun She, Yifan Song, Tim Weiß, Jens Greinert, Kevin Köser

GEOMAR Helmholtz Centre for Ocean Research Kiel, Wischhofstr. 1-3, 24148 Kiel

Abstract

Reliable quantification of natural and anthropogenic gas release (e.g. CO₂, methane) from the seafloor into the ocean, and ultimately, the atmosphere, is a challenging task. While ship-based echo sounders allow detection of free gas in the water even from a larger distance, exact quantification requires parameters such as rise speed and bubble size distribution not obtainable by such sensors. Optical methods are complementary in the sense that they can provide high temporal and spatial resolution of single bubbles or bubble streams from close distance. In this contribution we introduce a complete instrument and evaluation method for optical bubble stream characterization. The dedicated instrument employs a high-speed deep sea stereo camera system that can record terabytes of bubble imagery when deployed at a seep site for later automated analysis. Bubble characteristics can be obtained for short sequences of few minutes, then relocating the instrument to other locations, or in autonomous mode of intervals up to several days, in order to capture variations due to current and pressure changes and across tidal cycles. Beside reporting the steps to make bubble characterization robust and autonomous, we carefully evaluate the reachable accuracy and propose a novel calibration procedure that, due to the lack of point correspondences, uses only the silhouettes of bubbles. The system has been operated successfully in up to 1000m water depth in the Pacific Ocean to assess methane fluxes. Besides sample results we also report failure cases and lessons learnt during development.

Keywords: gas bubbles, bubble quantification, underwater vision, free gas

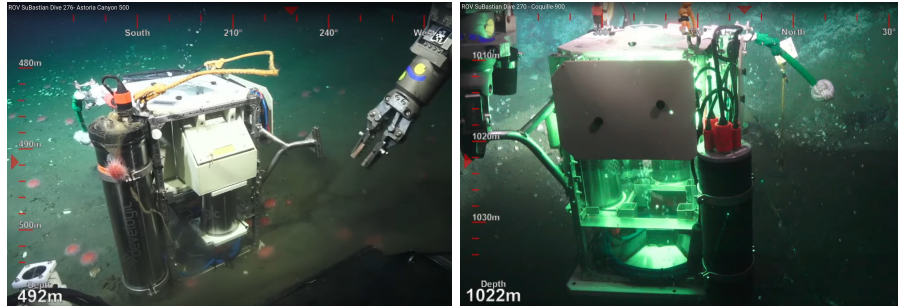


Figure 1: Instrument deployed by a deep sea robot in 500m and 1km water depth in the Pacific Ocean offshore Oregon during Falkor cruise FK190612 'Observing Seafloor Methane Seeps at the Edge of Hydrate Stability' (see also <https://youtu.be/fxiD75qmQFU> for a recording of the entire live stream captured by ROV SuBastian, Schmidt Ocean Institute). The instrument is positioned on top of a seafloor spot where methane escapes, then the bubbles rise through the instrument and are photographed by a wide baseline stereo camera setup at high frame rates for photogrammetric characterization.

characterization

1. Introduction

Greenhouse gases such as methane or CO_2 play a key role in climate change. At the ocean floor they can escape from natural reservoirs[1], or from leaky or abandoned drill or carbon storage sites, or participate in or result from chemical reactions, geological processes or microbial metabolism. Gas release, as well as formation and destruction of hydrates, can also influence the mechanical stability of seafloor areas, e.g. at continental slopes, and can have important impact on the local habitats. For all these reasons, exact quantification and monitoring of gas release from the ocean floor, as well as understanding the controlling conditions, are important research questions.

When released continuously from the seabed into the ocean as bubbles, methane and CO_2 form bubble streams that can rise towards the atmosphere[2] (see Fig. 2). Key quantification techniques for such free gas include physical collection of the gas with funnels, acoustical and optical methods, all of which

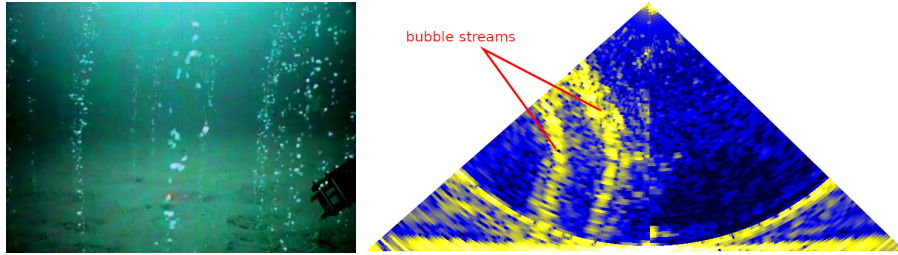


Figure 2: Methane escaping from the seafloor in the North Sea and forming bubble streams (left: horizontally looking ROV camera. right: multibeam echo sounder at a location with two bubble streams). The visual sensor can be positioned on top of one of these streams to capture the stream parameters such as rise speed and size distribution. Such streams can be detected also in ship-based echo sounders[3] as can be seen in the right image. Jointly, optical and acoustical observations can be used for large scale quantification. TODO: better picture ???

15 have advantages and drawbacks. Already a short-term, small-scale measuring of gas emissions with a collector is a challenging and costly task as it usually requires remotely operated vehicles (ROVs) to perform the mission and the volume measured is an integrative measure that does not provide information on individual bubbles. Long-term automated monitoring of gas seeps over a large

20 area using such a technique is unpractical. Since acoustical-based approaches can detect free gas underwater from a large distance, they have become the most efficient tools to find gas flux in a lake or a particular area of the ocean [4, 5, 6, 7] and to map gas activity over large areas[3]. However, exactly quantifying the gas flux requires prior knowledge of some essential parameters such

25 as the bubble size distributions and rising speeds [8, 9], which cannot be observed from the acoustic data itself. On top, these approaches require careful calibration, are sensitive to wavelength/size variations and noise and have limited spatial resolution [10, 3]. Quite complementary, rising bubble streams can be photographed by high speed cameras and characteristic parameters can be

30 obtained using photogrammetric techniques, which facilitates the acoustic inversions. In addition, visual information provides a better understanding of the bubble characteristics and behaviors, such as deformation and motion patterns

of the bubbles[10, 11].

Early works have focused on quantifying bubbly flow in a laboratory setup[12, 13, 14, 15, 10], where imaging and instrumentation conditions are much better
35 controlled than in the ocean. Fewer works exist that actually design and deploy in-situ imaging systems for the ocean, including telecentric lenses for very small bubbles [16], a monocular camera [11] and a small baseline stereo system [17]. All approaches require a lot of manual interaction to obtain bubble information,
40 and their focus was not on robust, automatic techniques that can work on gigabytes of image data. Consequently, extracting the bubble information from the video sequences accurately and robustly remains a challenging task and a complete and robust pipeline is required to automatically analyze many thousands of images that are obtained under uncontrollable, and often sub-optimal,
45 conditions.

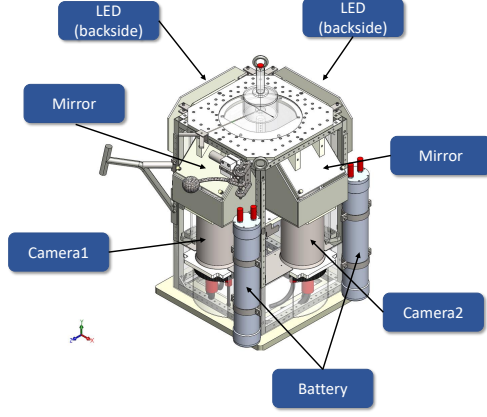
In this paper, we build on our preliminary lab studies for bubble measurements[10] and propose the following contributions: We (i) present a deep-sea wide baseline bubble measurement system, including a robust and complete pipeline that is able to automatically characterize bubble streams from long-term video sequences. We (ii) propose a new silhouette-based calibration ap-
50 proach that can adjust the calibration without point correspondences, i.e. only from bubble observations. We show that the same technique can be used for accurate bubble ellipsoid estimation. We (iii) carefully evaluate the system performance using ground truth measurements and show results and challenges on
55 real data acquired from deep sea missions up to 1000m depth.

2. Related Work

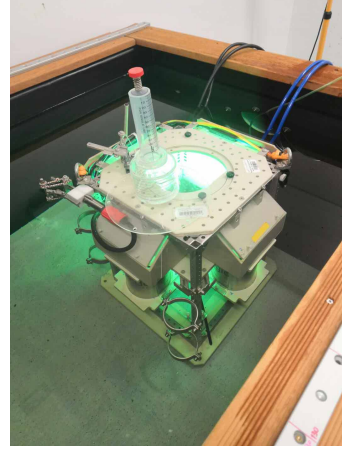
3D Measurement of Bubbles. Quantifying multi-phase flow parameters has been an interesting topic in many natural and industrial applications, and Particle Image Velocimetry (PIV) is a common technique to tackle such problems[18].
60 The gas/liquid flow is the basic scenario of two-phase flow, where the bubbles can be identified in the image sequences and the bubble features can be

extracted using 3D image processing techniques. Therefore in some laboratory-
 based works, special setups were built to photograph bubbly flow in a tube with
 high-speed cameras. These approaches generally consist of three major steps
 65 which include bubble identification, bubble 3D size measurement and bubble
 tracking over time. Zelenka et al. and Fu et al. [14, 19] have focused on the
 bubble outline extraction, but they both use a single camera to estimate the 3D
 volume of the bubble. Bian et al. [12, 13] assume the bubble is composed by
 two semi-ellipsoids and they have proposed an approach to extract the charac-
 70 teristic parameters of a single rising bubble from a pair of stereo images. The
 stereo camera system can significantly improve the 3D bubble size estimation
 but also poses other challenges, for instance, finding the correspondence of the
 same bubble in the stereo image pair. However, bubbles are not easily dis-
 tinguishable, and there is no rich texture information, consequently, traditional
 75 feature-based (e.g. SIFT[20]) or pixel-wise (e.g. SGM[21]) matching approaches
 can hardly be applied in this scenario. Therefore, lab approaches can often only
 reconstruct a single rising bubble. To save the second camera, and to avoid syn-
 chronization while sacrificing image area, Xue et al. [22, 15] have constructed a
 camera-mirror system, where the mirrors are used to generate a reflection of the
 80 bubble stream as seen from a different perspective. They have also proposed
 an equal-height heuristic to disambiguate multiple match candidates across the
 stereo image pair, making strong assumptions on bubble position. In a labora-
 tory environment, many complex setups can be built to better reconstruct the
 shape of the bubble. For instance, Fu et al. [23] have developed a space carving
 85 algorithm to reconstruct the free form surface of a single large rising bubble
 using multiple cameras. A similar system is developed by Masuk et al. [24] but
 with cameras and mirrors to create 4 virtual views for the space carving algo-
 rithm. These systems and algorithms are very attractive, but it can be difficult
 to transfer them into in-situ deep sea bubble stream characterization systems
 90 that can be used reliably in the ocean.

Optical Bubble Measurement Systems in the Ocean. Leifer et al.[16] have presented a deep sea optical bubble meter to analyze sizes and motions of bubbles with a single camera, and a manual workflow to extract the bubble volume according to the ellipsoid projection assumption is introduced. Using a telecentric
95 lens avoids scale ambiguity, but restricts the observation space to an extremely small volume. Later, Sahling et al.[25] develop an optical device and apply it to measure the gas discharge of a bubble stream using a perspective lens from a camera mounted on an ROV. Thomanek et al. [11] improved the system in terms of hardware design and proposed a more complete image processing
100 workflow to extract the bubble features. These works assume the distances of the bubbles to the camera to be constant, hence, the pixel-to-object scale can be calibrated using a ruler or reference. However, the bubbles in the ocean often rise in a zigzag way or the entire stream can bend with currents, consequently, the object distances can vary significantly. Also, large bubbles are
105 often not spherical, the extent of the bubble in the camera’s viewing direction is not observed then. Therefore, monocular systems can suffer from relatively large uncertainty when measuring the size and shape of a bubble. To address these issues Wang et al.[17] propose a short-baseline stereo camera system to obtain more 3D information, and later successfully deploy the system in an
110 expedition[26]. Jordt et al. [10] geometrically analyze the uncertainty of the triangulation estimation in a short-baseline stereo setup and proposed a novel 90° wide-baseline stereo camera system based bubble measurement setup and prove feasibility by lab experiments. This configuration can observe both the frontal and the side view of the bubble to remedy shape and distance uncertainty.
115 They also discuss things like image pre-processing, camera calibration considering flat port refraction [27, 28], bubble stereo matching and an ellipsoid fitting approach. While a complete workflow under ideal lab conditions is presented, and a prototype metal frame with GoPro cameras has been set up, the system was not evaluated in the ocean, where many challenges remain. Later,
120 She et al. [29] analyse replacing the flat port camera housings with dome ports, and discuss centering and calibration of the dome port cameras [30, 31]. In this



(a) Schematic System Overview



(b) System in Test Tank

Figure 3: (a), System overview and its technical description. (b) The system in an 80cm deep test tank.

contribution we build on top of this work and describe a practical deep ocean bubble measurement system, that, once positioned approximately on a bubble seep spot, captures bubbles using stereo photogrammetry. The system is robust
125 against inevitable nuisances such as dirt, disturbed illumination from upstirred sediment, offsets of the bubble stream, wobbly bubble ascent or temporal shift of the stream position. We provide automated methods for synchronization and robust background removal, as well as a completely new approach to instrument self-calibration without point correspondences: we use only the *outlines* of bub-
130 bles for wide-baseline recalibration from in-situ data. While previous systems have been qualitatively validated, we show a reconstruction accuracy of better than 1% when estimating the diameters of glass spheres sinking through the box that have a diameter of millimeters to centimeters.

3. System Design

135 3.1. Hardware Overview

Before diving into the gas flow quantification approach, we first summarize the deep sea in-situ bubble stream characterization instrument. The instrument follows the wide-baseline setting proposed in [10] and is a box shaped stereo recording device that can be deployed by a robot arm of an ROV as shown in Fig. 3b or can also be lowered from a surface vessel and then be positioned by divers. It contains a vertical corridor (64cm^2 cross section) in the box center which allows bubble streams rising through. Two deep sea titanium housings with dome ports are mounted at two adjacent sides of the box. Inside each of the housings, there is a high-speed machine vision camera recording images of $1024 \times$ 800 pixels resolution and a field of view of around 60° . The frame rate of the camera can be set to $80\text{Hz} - 100\text{Hz}$ (larger if smaller image areas are used), thus, each bubble can be photographed about 40 times since the bubbles can rise with a speed of $25 - 35\text{cm/s}$ [32]. Since both gas and water are largely transparent, the cameras can only observe refraction and reflection effects at the bubble surface, and previous studies[10] have shown that background illumination (also known as bright-field illumination in microscopy) is advantageous for photographing bubbles.

Therefore, two panels of green LEDs (550nm) are mounted at the camera-opposite faces of the box behind acrylic diffusor plates. They provide back-light illumination such that the outline of the bubble produces a dark rim in the image. Since each bubble is observed from 90° different perspectives, no photometric properties such as color or texture can be used for matching, and the outline in one camera only provides a weak hint about the size of the outline in the other camera and no explicit point correspondences can be obtained. A sample stereo image pair is shown in Fig. 4, where the left image and the right image are concatenated horizontally.

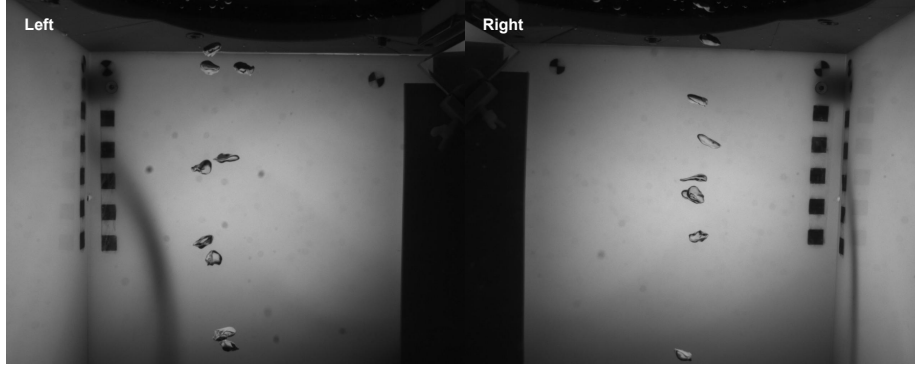


Figure 4: Sample stereo image pair captured by the instrument. The left image and the right image are concatenated horizontally (If not mentioned particularly, in the later figures, the left image and the right image are shown concatenated).

3.1.1. System Weight, Size, ROV-switch, Pressure-proof

The system size is 81cm (height, without funnel: 62cm) \times 43cm \times 43cm (see Fig. 5). The weight is about 60kg in air and 24kg in water. The box was designed to work at up to 1000m depth, but could be updated easily for use in up to 6000m, for which the main components, like the camera housings, are already built. The overall power consumption during 80Hz recording is 70W on average (100W peak during flash). It can be powered remotely or by battery, where the batteries last for 5h-10h of permanent flashing, depending on water temperature. Recording time can be extended as explained in the next paragraph.

3.1.2. Computers and Synchronization

The box consists of two pressure housings that each contain an intel NUC computer and a Basler Ace acA1300-200um machine vision camera behind a dome port. The 8mm C-Mount lenses (AZURE) have been carefully centered in the domes [30, 31]. We crop the images to 1024 \times 800 pixels to avoid frame-drops when writing to the 1TB SSDs inside each housing at high frame rates. The cameras are triggered by a micro-controller that starts exposure time and

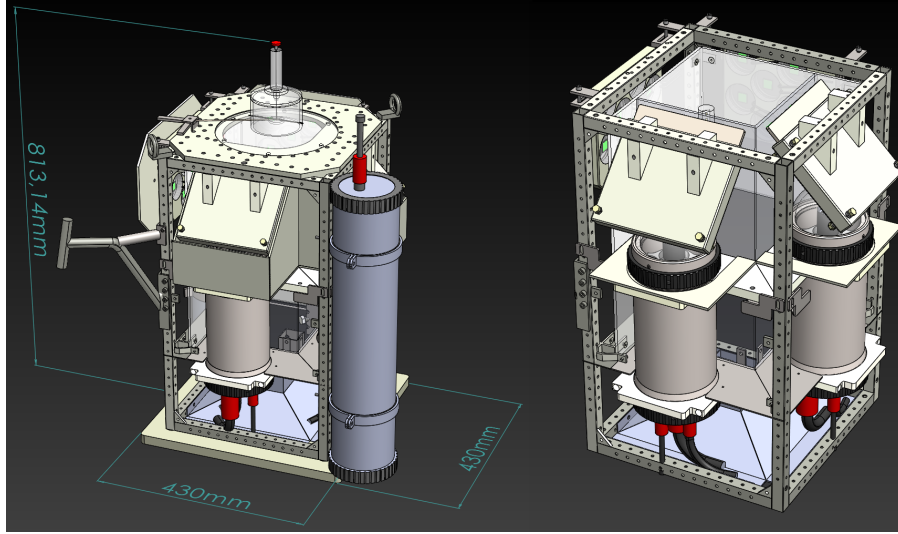


Figure 5: Left: Dimensions of instrument, including a removable collector funnel at the top. Right: virtual view into box, with some covers removed.

flashes on the rising edge of the trigger signal and stops exposure on the falling
 180 edge. Exposure time is set to 1ms to avoid motion blur. Every 5000 images,
 exposure and flash time is set to 10 microseconds only, which produces a black
 image in both cameras. These "black flash" images are exploited to synchronize
 the two streams. Before operation, the computer clocks are synchronized via
 network time protocol up to 1 second and we write the time stamp of the
 185 incoming image into the filename and save the raw image as pgm. At 80Hz the
 overall system currently produces a data rate of 1 gigabit per second or 0.45
 terabyte per hour. The images can be downloaded after the mission via gigabit
 ethernet which takes approximately the same time as taken for recording.

The box is equipped with a long-term-mode that modifies the microcon-
 190 troller's trigger signal. Rather than permanent mode, the microcontroller can
 create intervals such as the first five minutes of each hour. Outside these inter-
 vals LEDs are only flashed once every few seconds as a standby visualization.
 This reduces the storage needs by an order of magnitude and allows to operate

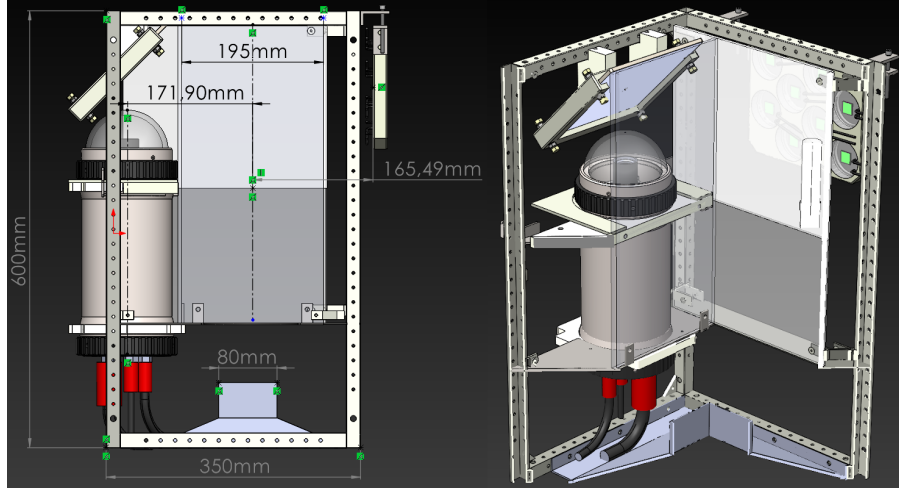


Figure 6: Left: Vertical section of the box showing the entrance funnel at the bottom leading to a 80mm wide square-shaped rise corridor. Right: Camera inside dome port looking through a mirror into the box. Also the background illumination for the other camera (not displayed here) using LEDs behind an acrylic plate is displayed.

the box for more than one day.

195 3.1.3. Cameras and Mirrors

As can be seen in Fig. 6, the rise corridor into which the bubbles are directed at the bottom is 8cm wide. The effective resolution is 5.7 pixel per millimeter in the center of the observation corridor. Since the camera housing is elongated, they are mounted vertically to the frame to save space, consequently, the cameras are looking upwards through two mirrors at roughly 45° angle to create
200 two virtual horizontal views.

3.1.4. Adjustment and Calibration

Each dome port camera is centered according to the method of [30] and it has been verified that refraction effects are insignificant in the observation corridor[31] and the perspective camera model can be used. After dome centering, we mount the stereo camera rigidly and perform stereo calibration. Due

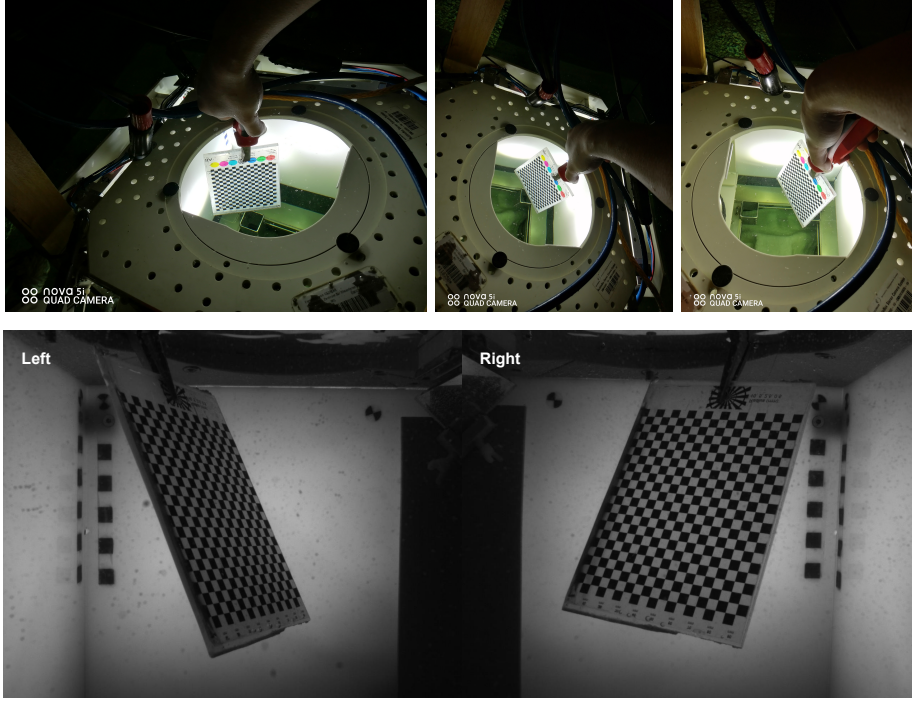


Figure 7: Stereo calibration of the instrument. Top: A calibration target is photographed by both two cameras multiple times underwater. Hence, the relative position and orientation as well as the camera intrinsics can be obtained. Bottom: sample calibration photos.

to the bright field setting, stereo calibration is performed underwater using a transparent calibration target within the bubble corridor. As shown in Fig. 7, both cameras observe the same target multiple times, and the camera intrinsics $\mathcal{K}_1, \mathcal{K}_2$ ¹ are calibrated using the traditional approach [33]. Note that the remaining tiny decenterings of the dome ports can be safely absorbed by distortion parameters as we are observing objects at a relatively fixed distance. Then, let the left camera be the origin of the world coordinate system as $\mathbf{T}_1 = [I_{3 \times 3} \mid \mathbf{0}]$.

¹Classically, the calibration matrix \mathbf{K} represents the perspective camera intrinsics such as focal lengths and principal points. For ease of notation we use the symbol \mathcal{K} to represent all intrinsics, including lens distortion parameters.

The right camera has the pose of $\mathbf{T}_2 = [R \mid \mathbf{t}]$. We can determine the pose of the right camera and do final refinement on both camera intrinsics by projecting the 3D target points onto the stereo images and minimizing the residuals between the projections and the identified corresponding points, as common for target-based calibration:

$$E = \sum_i^n \sum_j^m (\|\boldsymbol{\pi}(\mathbf{X}_i, \mathbf{T}_1, \mathcal{K}_1) - \mathbf{x}_{i,j}^1\|^2 + \|\boldsymbol{\pi}(\mathbf{X}_i, \mathbf{T}_2, \mathcal{K}_2) - \mathbf{x}_{i,j}^2\|^2) \quad (1)$$

Here, $\mathbf{x}_{i,j}^1$ and $\mathbf{x}_{i,j}^2$ indicate the i^{th} point on the target photographed by the j^{th} image, and the superscript ¹ and ² indicate the left camera and the right camera. $\boldsymbol{\pi}()$ represents the perspective projection function.

3.2. Bubble Stream Characterization Method

During in-situ operation, image data is recorded by the instrument. Processing is done afterwards using different modules written in C++ and CUDA, all of which can also run inside a docker-container on a remote server with GPU capabilities. In this case access works through a Jupyter Notebook interface. Automated, and efficient, processing is important, since we record more than half a million images per hour. After processing, the software is able to generate a report on the important bubble stream characteristics such as overall volume of gas released, bubble size distribution and rise velocity. In this section, we will give details on the approach for bubble stream characterization, and Fig. 8 illustrates an overview of the working pipeline.

3.2.1. Temporal Synchronization of Stereo Data

The two cameras are operated by independent computers and record time-stamped data. The time-stamps of the computers agree up to one, or for long-term deployments at most a few, seconds. Since the goal is to record with 80Hz-100Hz, we would need a clock agreement of less than 5ms in order to unambiguously associate matching frames in the recorded sequences. Therefore, every 5000 images, the micro-controller will generate a very short flash time (10 microsecond rather than 1000 microseconds), which leads to a black image.

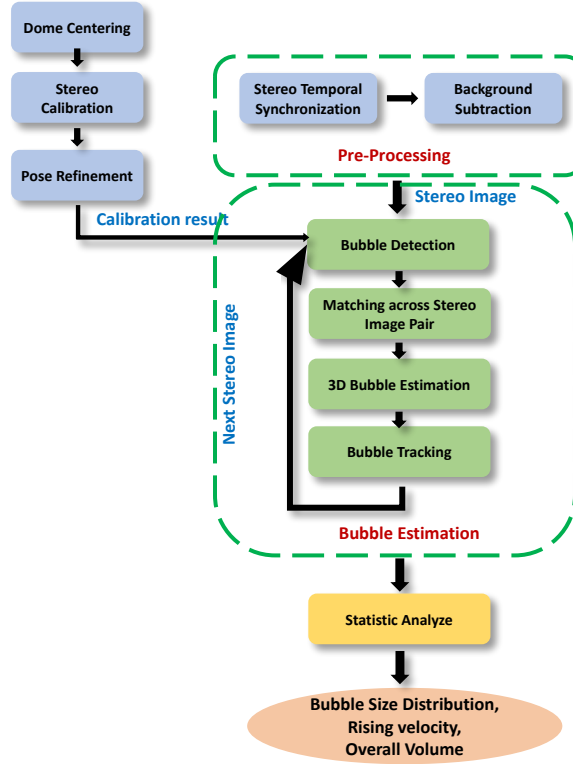


Figure 8: An overview of the automatic bubble stream characterization pipeline.

Those black images are now used as identifiers for synchronization of the two photo sequences. To achieve that, the software first iterates through both photo sequences and extracts the timestamp of each image and also detects the black images. This way the damage of potential frame drops in one camera is limited and the moment it happened can be detected easily. Next, the average time offset between the two computers can be calculated by the timestamps of the aligned black images. Afterwards, for each image in one of the sequences, we compute the expected timestamp when the corresponding image is captured, and then search the corresponding image in the other sequence by finding the minimum time difference. Finally, two photo sequences are aligned and a sequence of stereo image pairs is created. Particularly, when looking for black

images, we sample the main-diagonal and counter-diagonal pixels of the image and check their intensities. If all pixel intensities are smaller than 8 (empirical threshold), the image is considered a synchronization frame.

3.2.2. Background Learning and Removal

240 The original images usually contain complex background structures, for instance, sediments stuck on the dome ports, bubbles trapped and stuck somewhere and markers on the frame of the instrument, which makes bubble detection more complicated. But the background information can be learned and therefore removed if the background objects stay static in a certain time interval.

245 Assuming that we have only sparse bubble observations, at each pixel position in the image we will see the background in the majority of the images. Consequently, a robust temporal median filter algorithm can be leveraged to compute a background image from a series of bubbles images (see Fig. 9). Since the background can change over time, we apply the Median background estimation

250 using a sliding-window approach. We then subtract the 'learned' background image from each raw bubble image to obtain only the moving objects, i.e. the bubbles. In this step the images can also be radially undistorted, in case radial distortion is present. These steps can be implemented efficiently in CUDA using a streaming architecture.

255 3.2.3. Bubble Detection

Bubble detection aims at finding positions and 2D shapes of the bubbles in an image, more specifically, the bubble contours. Due to the back illumination, the bubbles appear as dark rims with a brighter area inside the contour in the foreground images. The image processing technique used here is similar to

260 [10, 11], first, the Canny edge detector is run to find those pixels and group them into edges. Then, the convex hull is determined for each bubble and an ellipse is fitted to the convex hull afterwards. The workflow of bubble detection is shown in Fig. 10. Since there are always single noisy pixels or dirt particles inside the water, a threshold for minimum sizes of bubbles has to be used. Since

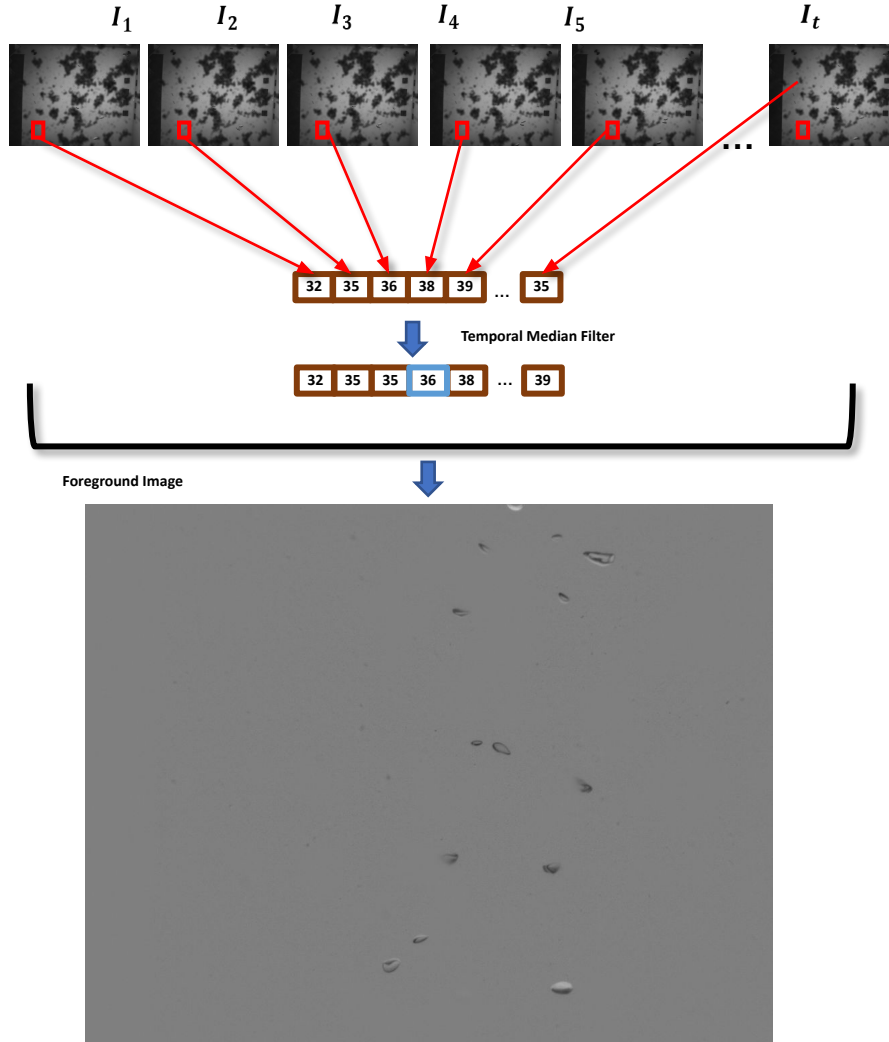


Figure 9: Principal of the temporal median filtering for background learning. If the background structures are stable in a certain time interval, they can be learned and removed by estimating the background image. For each pixel in the background image, the intensity value is determined by taking the median value along the temporal time series.

265 a 1mm-diameter spherical bubble corresponds to a circle of about 31 pixels circumference, the default setting is to reject contours with less than 30 pixels length as moving particles, in order to reduce mis-detection (see Fig. 10e). This

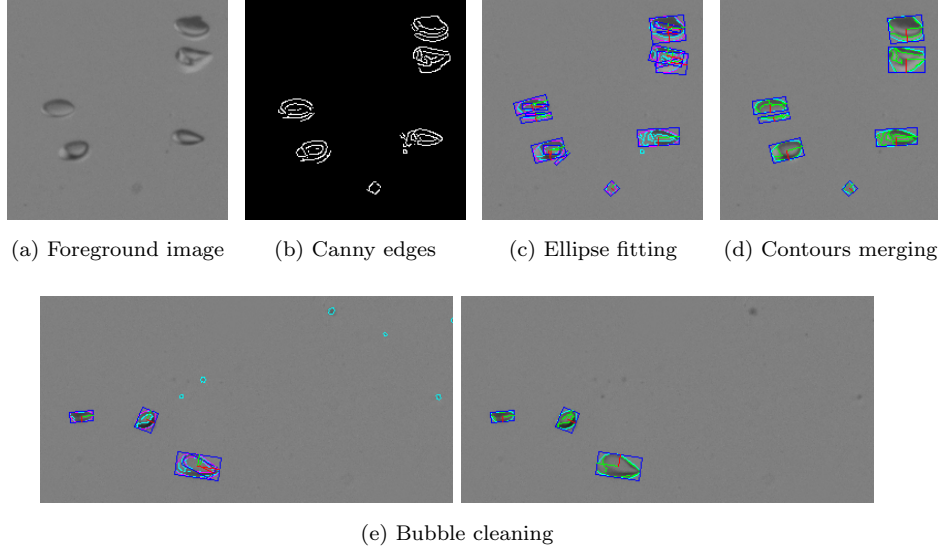


Figure 10: The workflow of bubble detection using image processing techniques.

can be adapted of course, e.g. when the goal is to measure very tiny bubbles in very clear water.

3.2.4. *Epipolar Geometry and Stereo Matching*

To estimate the volumes of the bubbles, it is required to find the corresponding bubble outlines across the stereo image pairs prior. Traditional feature-based [20] or pixel-wise [21] matching approaches find correspondences by computing similarity of local image patches. Since bubbles lack texture or other specific appearance information, only geometric constraints can be used for matching, such as epipolar geometry. As is shown in Fig. 11, a bubble is observed by two cameras, and the pose of the second camera with respect to the first camera is related by a rotation and translation R, t , which is obtained from stereo calibration. The second bubble's projection is therefore constrained by epipolar geometry. The matching we use is the same as described in [10], searching for candidates in a corridor around the epipolar line, and then solving the matching problem of all bubbles in an image pair at once using a bipartite graph.

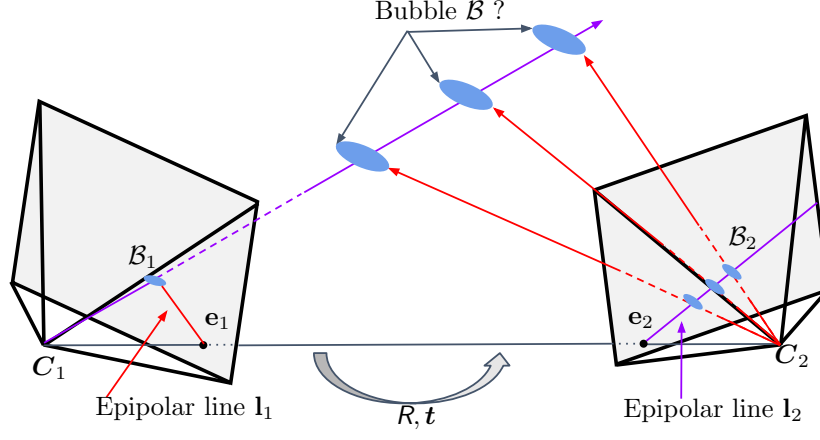


Figure 11: Epipolar geometry constraint for stereo bubble matching. The epipolar lines l_1 and l_2 are the projections of light rays seeing by the pixel B_2 and B_1 . C_1 and C_2 are the camera centers. The baseline between two camera centers and the light rays of a corresponding bubble span an epipolar plane. The epipolar constraint can reduce the searching space of the corresponding bubble.

After finding the bubble correspondences in the stereo image pair, we can estimate the bubble shape.

285 3.2.5. Ellipsoid Initialization

We model all bubbles in 3D as ellipsoidal, and initialize a 3D ellipsoid from the 2D ellipse parameters in the two images, before we optimize the 3D ellipsoid position and axes to fit both projections.

As can be seen from Fig. 12, the center of the ellipsoid is triangulated from the projection center of the ellipses, therefore, the distances of the bubble center to the cameras are also computed as d_1 and d_2 . Then, we specify a set of feature points $A_1, A_2, B_1, B_2, C_1, C_2$ as the end point of the ellipsoid axes, among which A_1, A_2 are back-projected from a_1, a_2 in the left image with a distance of d_1 . Similarly, B_1, B_2 are back-projected from b_1, b_2 in the right image with a distance of d_2 . The vector $\overrightarrow{A_1A_2}$ and $\overrightarrow{B_1B_2}$ form a plane, and the third vector $\overrightarrow{C_1C_2}$ is constructed as the cross product of the other two vectors,

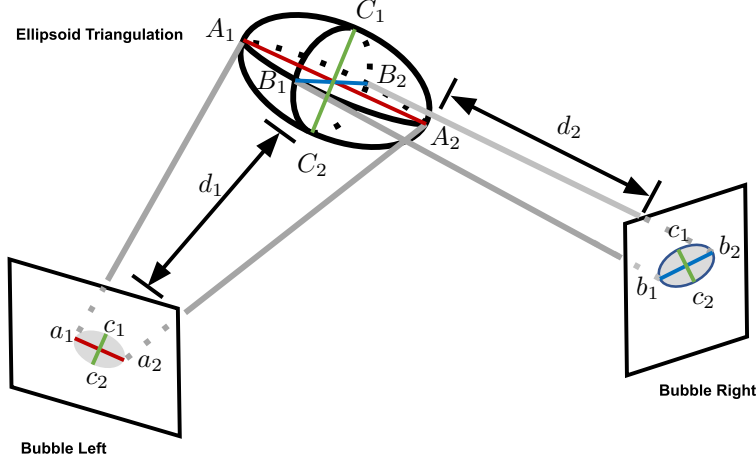


Figure 12: The principal of 3D ellipsoid triangulation from the stereo image pair.

such that $\overrightarrow{C_1C_2}$ is orthogonal to the plane. Since $\overrightarrow{A_1A_2}$ and $\overrightarrow{B_1B_2}$ are not orthogonal, we setup a 3×3 matrix R with three columns being these vectors, and map to a rotation matrix where the three columns are orthonormal. Then, we obtain the axes of the ellipsoid. Finally, we recompute the lengths of the axes by mapping the pre-computed feature points to the axis vectors, and the volume of the bubble can be obtained as:

$$V = \frac{4}{3}\pi abc \quad (2)$$

where a, b, c are the lengths of the ellipsoid axes.

290 Of course, the triangulated ellipsoid is an initial solution which can be refined further using bundle adjustment without point correspondences, which will be described in the next subsection.

3.2.6. Bubble Adjustment without Point Correspondences

We first represent the ellipsoid surface as a quadric, which is a 4×4 symmetric matrix \mathbf{Q} in the 3D projective space \mathbb{P}^3 [34]. The quadric can be initialized with

the triangulated ellipsoid parameters as following:

$$\mathbf{Q} = \mathbf{H}^{-T} \mathbf{Q}_u \mathbf{H}^{-1} \quad (3)$$

where $\mathbf{Q}_u = \text{diag}\{1, 1, 1, -1\}$ denotes the unit sphere. \mathbf{H} is the point transformation matrix which is composed by the orientation, translation, and the lengths of the ellipsoid axes:

$$\mathbf{H} = \begin{bmatrix} D_e & \mathbf{t}_e \\ \mathbf{0}^T & 1 \end{bmatrix} \quad (4)$$

where \mathbf{t}_e is the translation of the ellipsoid center, and D_e is:

$$D_e = \begin{bmatrix} a & 0 & 0 \\ 0 & b & 0 \\ 0 & 0 & c \end{bmatrix} \cdot R_e \quad (5)$$

with R_e being the orientation of the ellipsoid. Since we have calibrated the stereo camera system, we have obtained the camera intrinsics, as well as the camera poses, which are $\mathbf{K}_1, \mathbf{K}_2, \mathbf{T}_1, \mathbf{T}_2$. Therefore, we can construct the projection matrices of the stereo camera as $\mathbf{P}_1 = \mathbf{K}_1 \mathbf{T}_1$ and $\mathbf{P}_2 = \mathbf{K}_2 \mathbf{T}_2$. Now, given the projection matrix \mathbf{P} of a camera, the quadric can be projected onto the image as:

$$\mathbf{C}^* = \mathbf{P} \mathbf{Q}^* \mathbf{P}^T \quad (6)$$

where $\mathbf{C}^*, \mathbf{Q}^*$ is the dual conic of \mathbf{C} , and dual quadric of \mathbf{Q} respectively, and they can be obtained through:

$$\mathbf{Q}^* = \mathbf{Q}^{-1} \quad \mathbf{C}^* = \mathbf{C}^{-1} \quad (7)$$

Therefore, we can project the triangulated ellipsoid to the left image and the right image and obtain their 2D conics \mathbf{C}_1 and \mathbf{C}_2 . To optimize the quadric, we minimize the difference between the projected conics and the detected conics. Since we have detected the bubble and fit an ellipse around the contour in Sect. 3.2.3, we sample points on the ellipse uniformly and define the cost function as the Mahalanobis distance of the sampled points \mathbf{x} (lens distortion was removed

in the background removal step) to the conic:

$$\mathbf{x}^T \mathbf{C} \mathbf{x} \quad (8)$$

Therefore, the optimal quadric \mathbf{Q} can be solved via minimizing the following:

$$E = \sum_i \|\mathbf{x}_{i,1}^T \mathbf{C}_1 \mathbf{x}_{i,1}\|^2 + \|\mathbf{x}_{i,2}^T \mathbf{C}_2 \mathbf{x}_{i,2}\|^2 \quad (9)$$

where $\mathbf{x}_{i,1}$ and $\mathbf{x}_{i,2}$ are the sampled points on the detected ellipse in the left im-
 295 age and the right image. After optimizing the quadric, we retrieve the ellipsoid
 parameters from the quadric representation.

3.2.7. Bubble Tracking

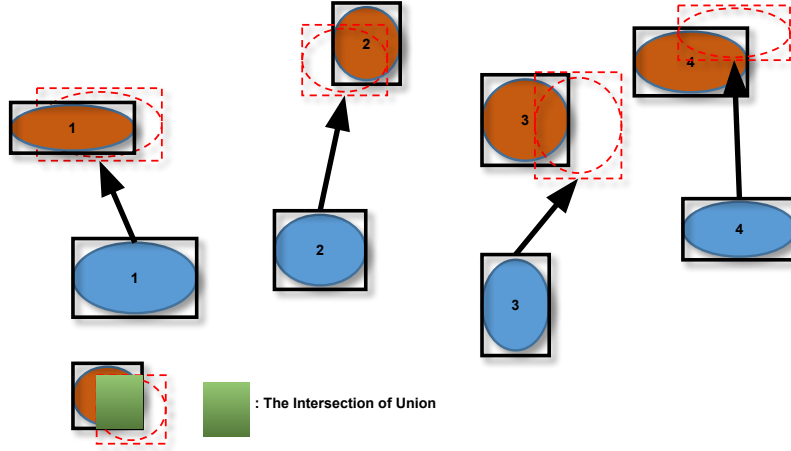


Figure 13: The principal of the data association step in the bubble tracking. The blue ellipses denote the bubbles in the current frame, the brown ellipses represent the identified bubbles in the next frame. The IoU is computed between the predicted and detected bounding box.

To measure the rise speed of each bubble, and also to avoid multiple count-
 ings, the bubbles need to be tracked over the image sequence. We utilize the
 300 Tracking-by-Detection [35] framework to address this issue where the interest-
 ing target is identified in each frame and associated with its previous trajectory.
 Therefore, the tracking problem is essentially converted to a matching prob-
 lem which is similar to Sect. 3.2.4. The bubbles always rise upwards with a

small oscillation in the sideward direction, which can be used as a constraint
 305 to reduce the search space in the data association step. In this contribution,
 we employ the SORT (Simple Online and Realtime Tracking) tracker [36]. The
 bubble position in the next frame is first predicted by a Kalman Filter that
 holds each bubble’s parameters, then the IoU (Intersection of Union) is utilized
 as the weight for constructing the bipartite graph.

310 To assign the newly identified bubbles to their previous trajectories, we treat
 the bubbles in the current frame as the source group and the new bubbles in the
 next frame as the target group, and construct a bipartite matching graph like
 in Sect. 3.2.4. To impose the upwards and the sideward motion constraints, we
 discard the edges where the new bubbles are below the old bubbles, and also
 315 discard the edges where the sideward motion exceeds a threshold. Then, for
 each bubble in the current frame, its expected position and bounding box are
 predicted by the Kalman Filter, and we compute the intersection area of union
 (IoU) between the predicted bounding box and the new bubble, and use it as
 the weight of the edge in the graph. As illustrated in Fig. 13, the IoU expresses
 320 the similarity between the predicted bubble and the detected bubble. Finally,
 the best matches from the next frame to the current frame can be found via
 the Hungarian algorithm. For those bubbles which have no assignment to the
 previous trajectories, new trajectories are initialized.

3.2.8. Counting at Reference Surface

325 To avoid multiple counting of the bubbles, and to treat fast and slow rising
 bubbles in a consistent manner, we only count a valid bubble and calculate its
 characteristics when its trajectory passes a virtual horizontal plane, the counting
 reference surface. This surface is defined by selecting a certain image row in the
 first camera. Consequently, we disregard bubble trajectories that start above the
 330 counting reference surface or bubbles that dissolve before reaching the reference
 surface.

4. Evaluation

4.1. Recalibration by Bubble Adjustment

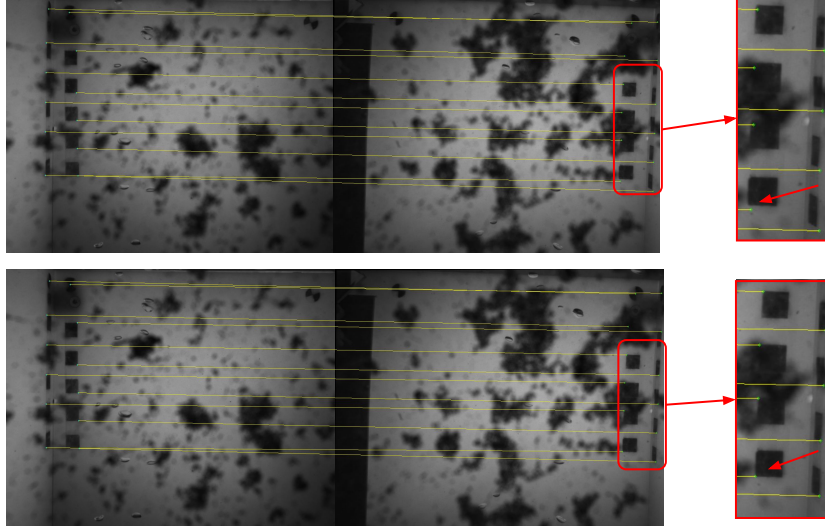
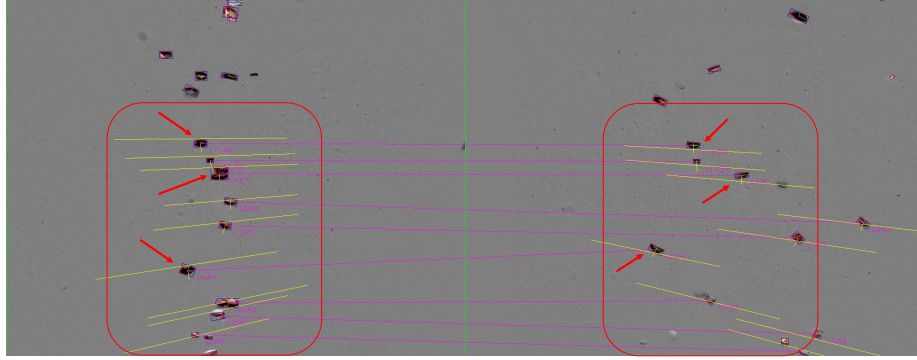
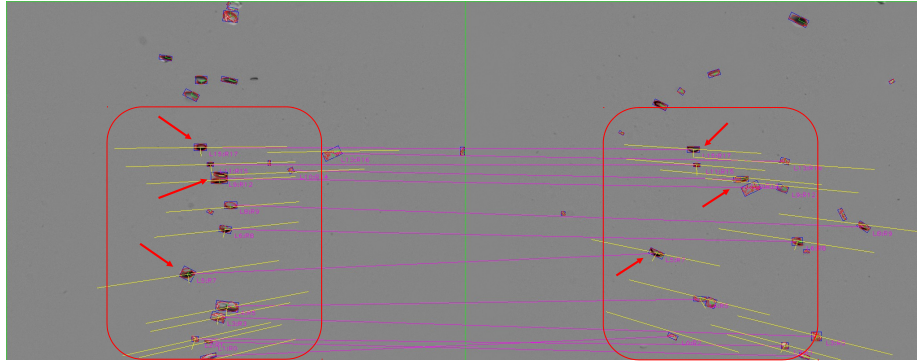


Figure 14: Top: Before recalibration, the projections of the square photogrammetric markers are off from their true positions. Bottom: After recalibration, the projections match the actual image.

One lesson learned from the actual deep sea experiment is that the relative
335 orientation and position of the stereo camera system could vary due to significant environmental changes. Under extremely high water pressure and very low temperature, the metal frames and the plastic panels where the cameras and the mirrors are mounted can behave different from the water pool in room temperature, where we perform the stereo camera calibration step. Therefore
340 the results are not directly applicable to the deep sea environment, which can be proved by comparing the stereo images acquired in the water pool and the in-situ data. As shown in Fig. 14 top, the black square photogrammetric markers are attached rigidly to the acrylic panels and they are both visible by the stereo cameras. Since we know the ground truth positions of the markers, we
345 can project the outer corners of the markers onto the images using the stereo



(a) Before recalibration



(b) After recalibration

Figure 15: Top: Before recalibration, the epipolar lines are off from the corresponding bubbles. Bottom: After recalibration, the epipolar lines intersect with the corresponding bubbles.

calibration results obtained in Sect. 3.1.4, and it is clear that the projections are off from the in-situ images (see the red arrows). Similarly, the stereo epipolar matching results have shown that the epipolar lines of the bubble contour masses are tangent to the corresponding bubble outlines (see Fig. 15a). Consequently, a recalibration is necessary, however, performing in-situ calibration is infeasible. Therefore, we propose a self-calibration approach to refine the relative orientation and translation of the stereo cameras utilizing directly the

in-situ images.

The self-calibration is essentially an extension to Sect. 3.2.6 where we use bundle adjustment with ellipse constraints to optimize the quadric representation of the bubble. Now, leaving the cost function untouched, we add multiple bubbles (quadrics) into the equation system (see below) to jointly optimize all quadrics and the relative orientation and position of the stereo camera.

$$E = \sum_k \sum_i \|\mathbf{x}_{i,1}^T \mathbf{C}_1^k \mathbf{x}_{i,1}\|^2 + \|\mathbf{x}_{i,2}^T \mathbf{C}_2^k \mathbf{x}_{i,2}\|^2 \quad (10)$$

now, \mathbf{C}_1^k and \mathbf{C}_2^k are the 2D conics projected from k^{th} bubble (quadric) in the left and right image. By accumulating multiple bubbles from multiple frames,
 355 we can re-calibrate the stereo camera system and resolve the environmental change issue (note that we don't need to track those bubbles in this scenario).

As can be seen from Fig. 14 bottom and Fig. 15b that the projections of the photogrammetric markers are in the correct positions, and the epipolar
 360 lines of the bubble contour masses now intersect with their corresponding bubble outlines.

4.2. Dark Frames

We have verified that the dark frame detection works robustly and reliably. Using a frame rate of 80Hz we do not observe frame drops, and we can see in the
 365 image counters that a dark frame appears every 5000 images. At 100Hz frame drops appear rarely. In Fig. 16 we exemplify the dark frame detection and the timing during a short experiment of taking about 40000 images in both cameras at 80Hz. Before the experiment, we deliberately did not synchronize the clocks of the two computers and they differ about 2.7 seconds. We subtract both the
 370 frame counters and the timestamps recorded independently by both computers when a black frame is detected. It can be seen that the counter difference is constant, whereas the time is almost constant, but drifting slightly. For this short experiment that takes 437.5 seconds, we observe a clock drift between the two computers by 1.3ms, which means 0.27 seconds per day. Since the frame
 375 counter offset stays stable at the detected dark frames we can still associate

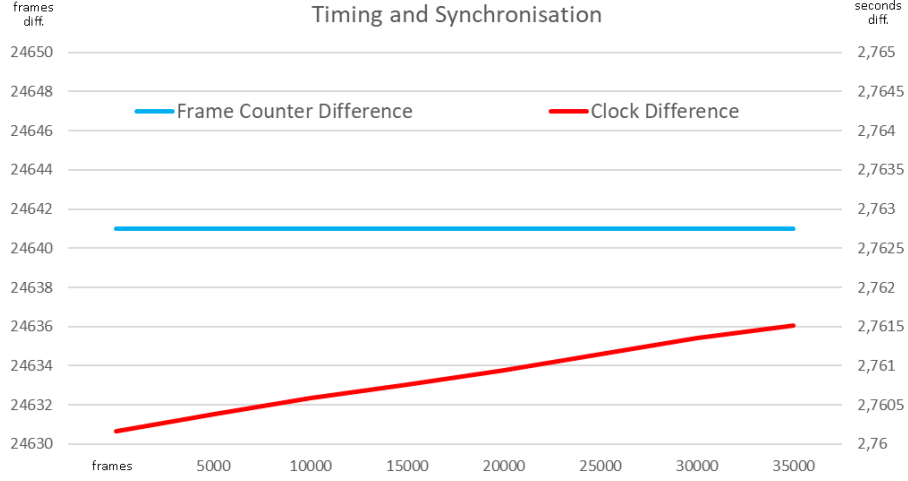


Figure 16: Frame offset measured by black frames (top / blue curve) and clock difference of the computers in seconds (bottom / red curve). We observe that the black frames are detected reliably and no frames are lost. However, the recorded time stamp difference increases slightly due to clock drift.

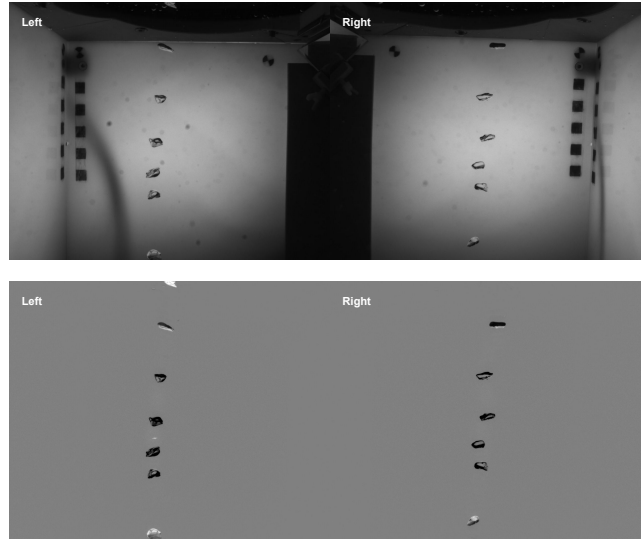
the correct images and they were triggered at the same time. However, one of the computer’s clocks runs 0.0005% faster than the trigger signal, the other one 0.0002%. For computing the rise speeds and flow rates, this consistency is by far good enough.

380 4.3. Background Removal

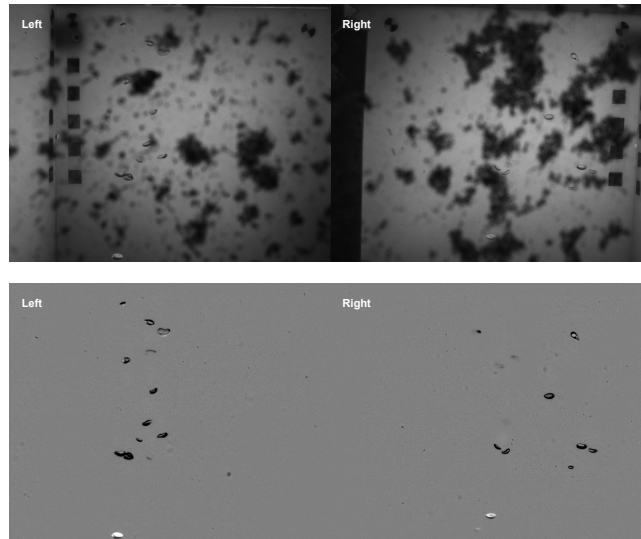
Fig. 17 shows two sample results of the background removal from two different data sets. As can be seen that the temporal median filtering algorithm works perfectly when the water body is clean and clear (see Fig. 17a), and it is also evidently that the algorithm is robust enough to cope with images like in
 385 Fig. 17b where sediments stuck on the camera housings and block part of the cameras’ view.

4.4. Known Reference Objects

To evaluate the accuracy of the proposed ellipsoid triangulation technique and later bundle adjustment with ellipse constraints, we first conduct an experi-



(a) a



(b) b

Figure 17: Two sample results of the background removal. In each sub-figure, the top row shows the original stereo images and the bottom row shows the resulting foreground images.

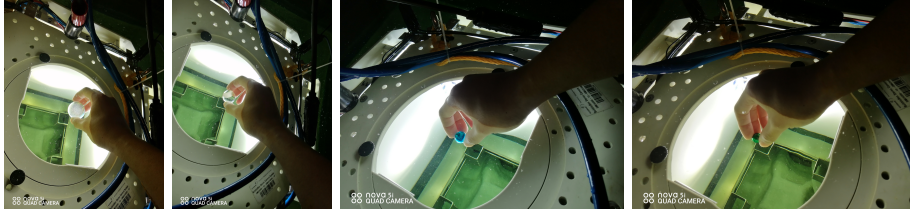


Figure 18: Evaluation on the known reference objects (4 glass marbles with different radiusses).

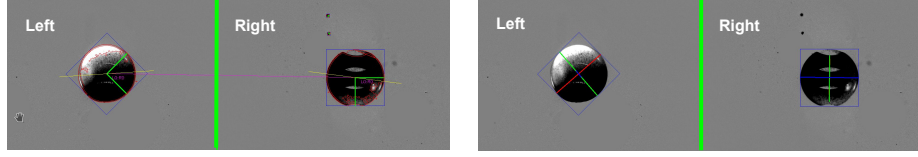
Table 1: Evaluation results of the glass marbles.

	proposed method [mm]	vernier caliper [mm]	err. [%]
Marble R17	34.33 ± 0.09	34.72 ± 0.10	1.12
Marble R13	25.00 ± 0.20	25.10 ± 0.01	0.39
Marble R8	16.01 ± 0.16	15.91 ± 0.25	0.63
Marble R6	12.68 ± 0.16	12.41 ± 0.13	2.2

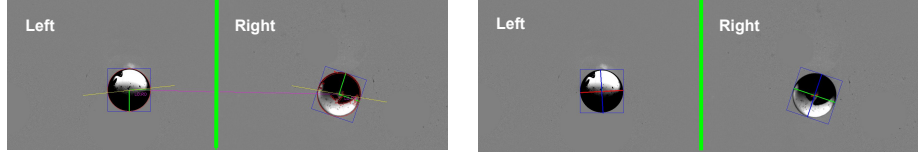
ment using the instrument to photograph glass marbles of approximate radiusses
6mm, 8mm, 13mm and 17mm, falling through the corridor of the instrument in
water (see Fig. 18). The diameter of each marble were measured by a vernier
caliper. Since the marbles are also not perfectly spherical, to obtain an accurate
reference, we measure each glass marble 10 times while rotating it and use the
average diameter as the reference. Next, we drop each glass marble through the
corridor of the instrument 10 times to obtain over 100 samples. Then, we per-
form bubble detection, epipolar geometry matching, ellipsoid triangulation and
bundle adjustment on images where we can see and identify the glass marbles,
and the evaluation results of the equivalent diameter ² are shown in Tab. 1.

It is clearly shown that the estimation accuracy of a known reference object
is in the range of 1 – 2% in the equivalent diameter under ideal conditions.
Some sample intermediate results can be found in Fig. 19, where the epipolar

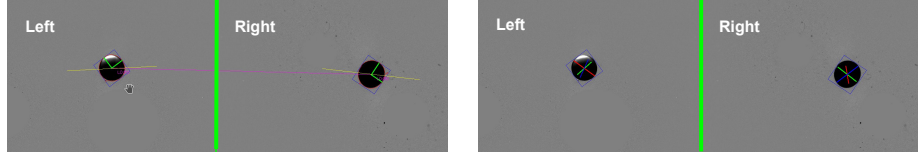
²The equivalent diameter of a non-spherical particle is equal to a diameter of a spherical particle that exhibits identical properties to that of the investigated non-spherical particle.



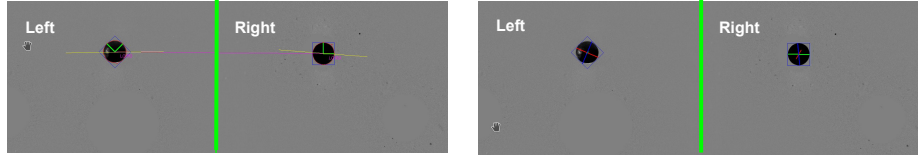
(a) Glass marble R17 (radius $\approx 17\text{mm}$)



(b) Glass marble R13 (radius $\approx 13\text{mm}$)



(c) Glass marble R8 (radius $\approx 8\text{mm}$)



(d) Glass marble R6 (radius $\approx 6\text{mm}$)

Figure 19: Sample intermediate results of the known reference objects evaluation (The stereo images are concatenated into one image). From top to bottom: selected one sample for each glass marble. From left to right: stereo epipolar geometry matching and the re-projected ellipsoid. In the left part of each sub-figure, the glass marbles are identified and marked as red outlines and a blue bounding box; The lilac lines connect the bubble correspondences and the yellow lines are the epipolar lines of the contour mass in the other image (Note that the contour masses of the corresponding bubbles are not corresponding points). In the right part of each sub-figure, the final reconstructed 3D ellipsoid is projected onto the image, and its X -, Y -, Z - axis are shown in red, green, blue lines respectively.

geometry matching results are shown in the left part of the sub-figures, while the re-projected ellipsoids are shown in the right. Here, to re-project an ellipsoid,

Table 2: Bubble stream characterization results of the controlled experiments.

	gas flow	occlu- sions	duration	cylinder read [ml]	estimated vol.[ml]	volume err.[%]	eq.radius err.[%]
1	low	no	7 min	81	84.4	4.2	1.4
2	med.	no	1 min	105	109.2	4.0	1.3
3	high	yes	50 sec	110	121.1	10.1	3.3
4	higher	many	30 sec	135	188.12	39.35	11.2

we first project its center point onto the image, and project the 6 end points of the ellipsoid axes and then connect them.

4.5. Controlled Experiments

Next, to demonstrate the effectiveness of the complete workflow, we first conduct a controlled experiment. We set up the instrument in a water pool with an air-bubble generator attached underneath the instrument. The generator is able to produce air bubbles at different flow rates with different sizes to control the density of the bubble stream. A cylinder is used to collect the released gas bubbles on top of the instrument and to measure the overall volume. The instrument records photos of the rising bubbles as if it was in the ocean, and the image sequences are analyzed by the bubble stream characterization approach which is proposed in Sect. 3.2. Then, we compare the estimated overall volume with the cylinder measurement. To evaluate the accuracy and robustness of the bubble stream characterization approach, we start with low bubble stream density and gradually increase the gas flow of the bubble generator. An overview of the sequences can be seen in Fig. 20, and the experiment results are shown in Tab. 2.

As can be seen from Tab. 2, when there is only one single bubble plume, the overall volume estimation is accurate as it shows a relative volume error of 4.2% (sequence 1) and 4.0% (sequence 2). Since the volume increases with the third power of the radius, this can be interpreted as an equivalent radius error

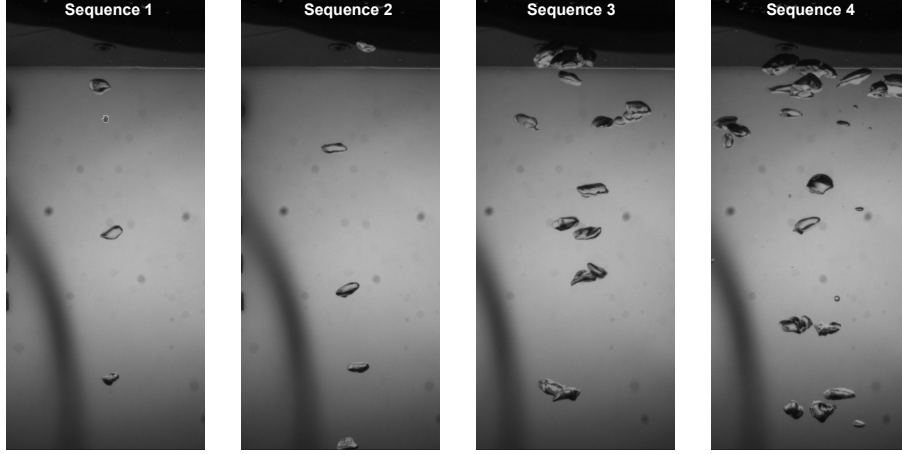
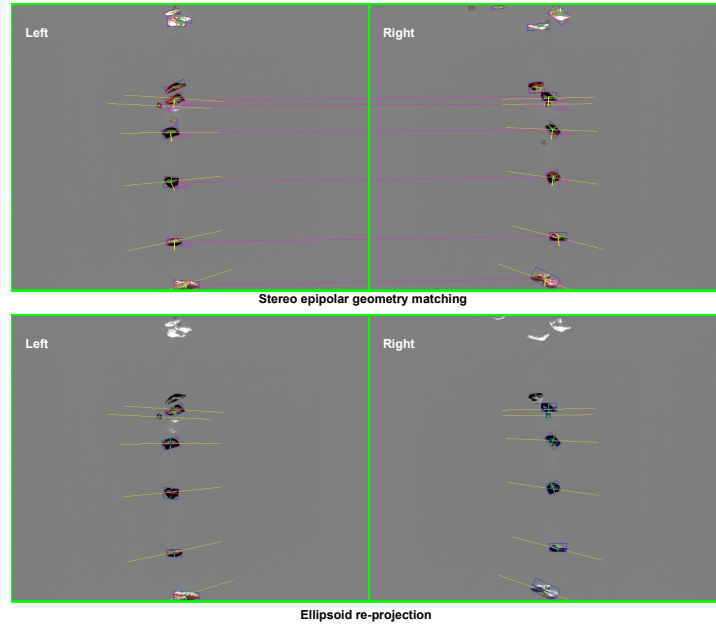
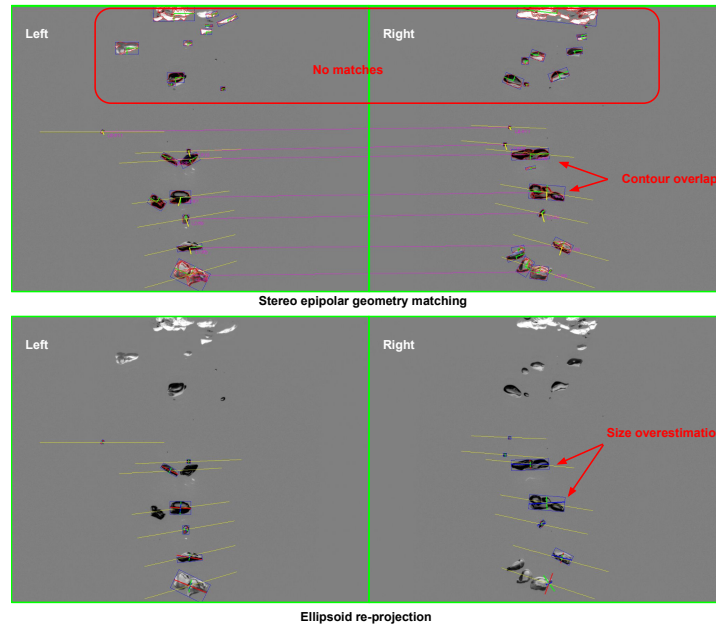


Figure 20: An overview of the sequences for the controlled experiments.

of slightly more than 1%, which is close to the glass marble experiment results and also shows that the ellipsoid model assumption works well in this bubble size range. The sample intermediate results are shown in Fig. 21a, and it can be seen that the ellipsoid re-projections well fit the identified bounding boxes of the bubbles. But we can see that the accuracy decreases with increasing flow rate due to bubble contours overlapping in the image, especially in sequence 4 where the bubble stream density is too high. One explanation is that the overlapping contours in the image are merged into a bigger contour which encloses the bubble cluster such that the ellipsoid size is overestimated. In addition, it also introduces ambiguity both in stereo epipolar matching and bubble tracking (non-equal number of bubbles identified, see Fig. 21b), which also adds error to the final volume estimation. Nevertheless, for a moderate amount of overlapping bubbles in the image (like in sequence 3), we still obtain a result of an overall volume error of 10% (or, equivalent radius error of around 3%). Note that also the physical collection of the gas comes with some uncertainty. In particular for the more turbulent high flow rate sequences 3 and 4 a few bubbles already stick to the cylinder entrance and do not get collected, and also the cylinder measurement has some uncertainty (surface tension, different water pressure leading to different gas expansions). We therefore consider an overall volume



(a) Medium bubble density (sequence 2)



(b) High bubble density (sequence 4)

Figure 21: Sample results of stereo epipolar geometry matching and ellipsoid re-projection from the controlled experiments.

Table 3: Sample results of bubble stream characterization on data from the Pacific Ocean.

date, time	count	volume [ml]	flow rate [ml/s]	diameter [mm]	velocity [cm/s]
06/19, 16:50	370	40.33	0.646	5.71 ± 0.51	26.21
06/19, 17:05	349	36.78	0.591	5.70 ± 0.50	26.33
06/20, 09:09	453	37.31	0.591	5.20 ± 0.62	28.22
06/20, 09:24	462	33.93	0.565	5.00 ± 0.60	28.65
06/20, 19:11	544	41.97	0.699	5.03 ± 0.56	27.79
06/20, 19:26	520	41.13	0.685	5.08 ± 0.54	27.86

445 difference of about 10% still a reasonable agreement.

4.6. Data analysis from the Pacific Ocean

The instrument has been deployed in the Pacific Ocean during Falkor Cruise 'Observing Seafloor Methane Seeps at the Edge of Hydrate Stability' (FK190612), jointly with several other instruments to analyze bubbles and hydrate. A detailed analysis of the observations of the scientific cruise is out of the scope of
450 this paper and will be discussed in [37]. Instead, we only exemplify some results here. The instrument was deployed at the seep sites by an ROV (also see Fig. 1). We selected 6 sequences from a few interesting time points and report the evaluation results in Tab. 3.

Bubble stream characterization

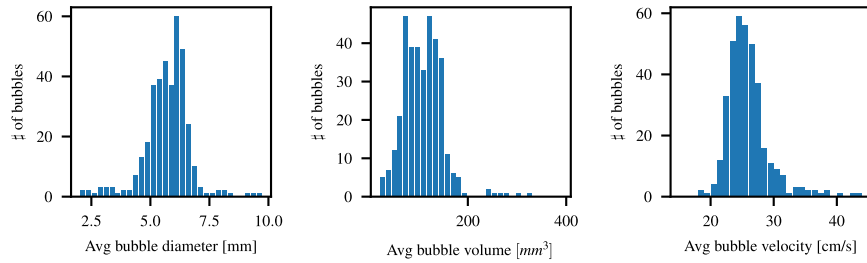


Figure 22: Bubble stream characterization results for sequence 06/19, 16:50.

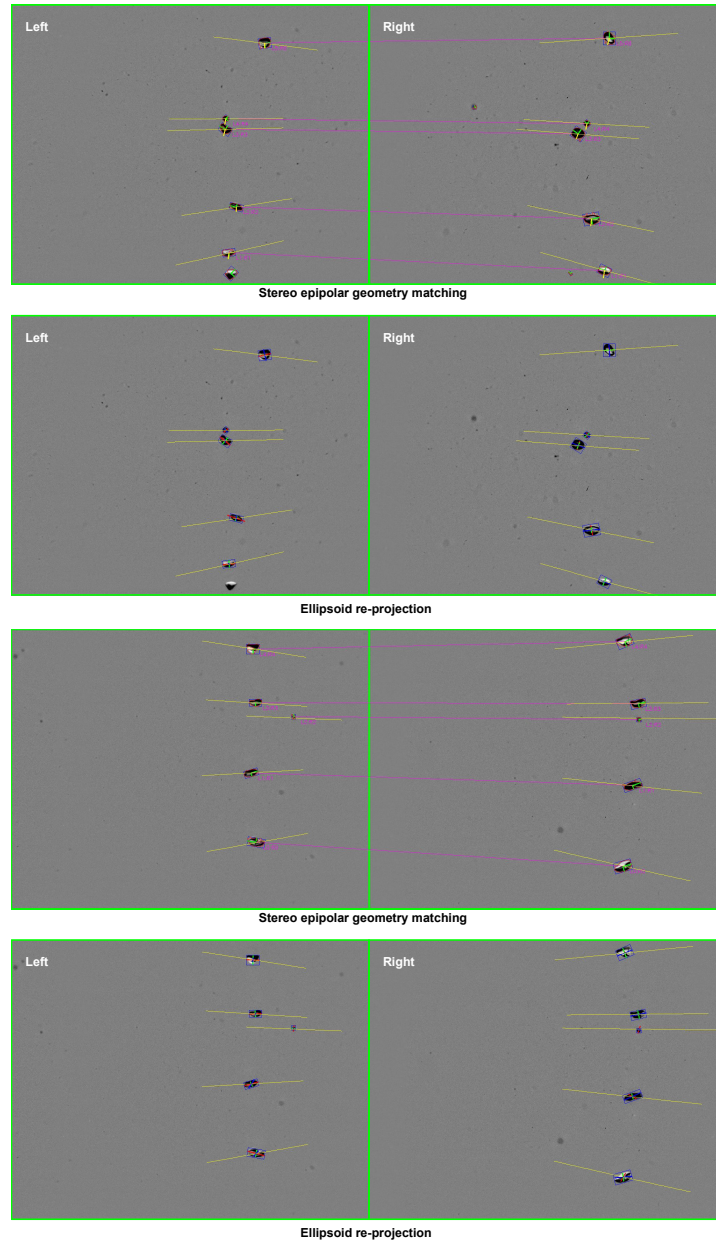


Figure 23: Sample results of stereo epipolar geometry matching and ellipsoid re-projection for sequence 06/19, 16:50.

455 Particularly, we show the bubble stream characterization results and some
sample intermediate results for the first sequence in Fig. 22 and Fig. 23. It
is clear that the algorithm is able to find correct bubble correspondences, and
the re-projected ellipsoids are well located inside the bounding boxes of the
identified bubbles. Since it is very difficult to obtain a ground truth reference for
460 the estimated bubble streams, we also positioned a scale-bar board in-situ right
next to the bubble streams as a second examination, although we understand
that this is only a weak validation, it cannot provide an accurate reference.
Still, by calculating roughly the bubble radiusses and the rising velocity, we
have verified that our estimation is in a reasonable range.

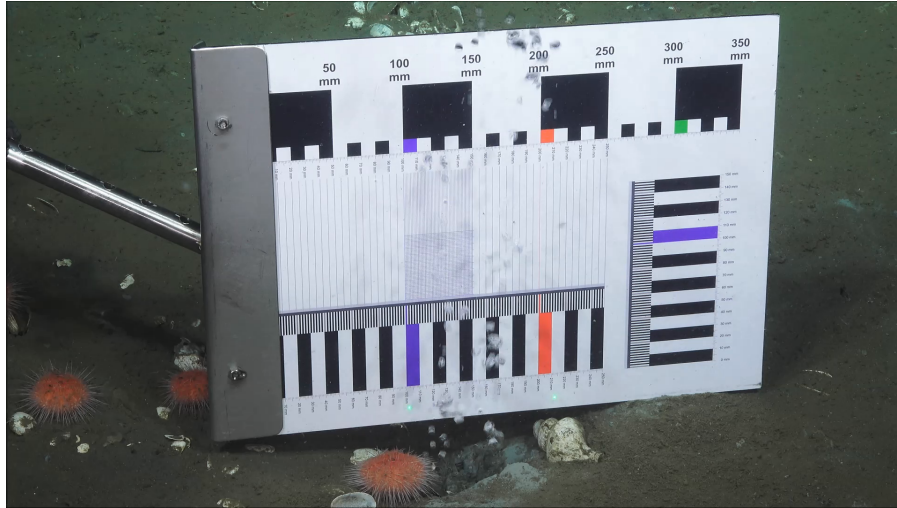


Figure 24: A scale-bar board was used to roughly examine the estimated bubble sizes and rising velocity. Picture taken by ROV SuBastian, Schmidt Ocean Institute.

465 5. Discussion

Both the real data as well as the ground truth experiments indicate that
the overall approach works well in the deep sea and the measurement process
is robust even in presence of dirt and other nuisances. The achieved accuracy
under good conditions is much better than can be expected from monocular

470 methods. However, there are some limitations and failure cases in practical applications:

Both Cameras Must See the Bubbles

For stereo evaluation, both cameras have to see every bubble. In case the view of a single cameras is blocked by an animal, or the water is too turbid, 475 the stereo matching procedure fails (see Fig. 25a). Also, in case the box is not deployed in an upright orientation, e.g. at a slope or in case it sinks into the sediment, bubbles will not rise exactly through the corridor and might get out of sight for one of the cameras, as shown in Fig. 25b. In this case single view approximations (shape and position assumptions) have to be used. In future 480 versions we will use a wider image, and not crop it strictly to the 8cm corridor that works well only in lab conditions. This should increase robustness further.

Density of Bubble Stream

The entire system is designed for a stream of bubbles where bubbles rise one by one. In case multiple or many bubbles are seen at the same height, they 485 tend to occlude each other and it is difficult to disambiguate the bubbles. In this case small bubbles tend to be overlooked, which might bias the bubble size distribution, whereas the overall flow will probably only be slightly affected.

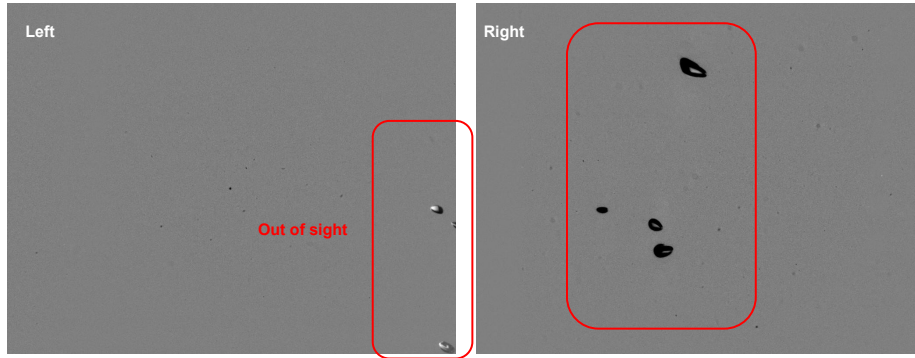
The opposite problem occurs in case the water contains many small dirt particles (e.g. upstirred sediment). From a geometrical point of view they are 490 difficult to distinguish from small bubbles, so a minimum bubble size threshold was used. This is a general specificity versus sensitivity problem. Potentially, a solution could be to learn motion patterns and appearances, but this might not generalize to previously unseen ocean locations.

Technical Limitations

495 A current limitation of the instrument is that it is still using too much power in standby-mode since only the flashes are disabled during standby, but the computers are still running. This limits maximum runtime. Similarly, recording full images rather than saving only the bubbles quickly fills the storage space. We



(a) Failure case 1



(b) Failure case 2

Figure 25: Failure cases. (a) Left, a sea urchin is sitting on the dome port. Right, a large piece of sediment is blocking the camera's view. (b) The bubble stream does not rise upwards, due to the instrument standing on a slope or is sunken into the sediment. When the bubbles get out of sight for the left camera stereo quantification does not work any more, and one has to use single view approximations.

have tried an experimental real-time encoding using live background subtraction, but processing 0.8 gigapixel per second reliably is at the performance limit
500 of the current hardware and capturing data at sea is so expensive that we decided not to risk deleting the raw data.

6. Conclusion

We presented and discussed a robust photogrammetric bubble stream characterization system for deep ocean deployment. The overall system has been
505 deployed in up to 1000m water depth and was used to quantify methane fluxes offshore Oregon. In a test tank we have verified the accuracy of the bubble radius estimation to be correct up to very few percent using hand-measured glass marbles and an air bubble test with the gas additionally collected by a funnel. Besides the robust steps we have also presented a new calibration procedure
510 that does not rely on point correspondences, but works with silhouettes in a wide baseline setting.

Acknowledgments

The authors would like to thank Matthias Wieck, Jan Sticklus, Eduard Fabrizio
515 rizius and Thorsten Schott for co-designing and constructing the many components of the systems. Early ideas about building a bubble measurement device reach back to discussions with Anne Jordt, Peter Linke, Matthias Haeckel and Reinhard Koch, and a preliminary prototype has been built with Jens Schneider von Deimling. We would particularly like to thank Anne Jordt and Claudius Zelenka for providing the software from [10] and many fruitful discussions. We
520 are grateful to Lasse Petersen for providing the CUDA tool for background removal and Furkan Elibol for dockerization and the Jupyter notebook interface. This work has received funding from Deutsche Forschungsgemeinschaft DFG (German Research Foundation) through the Emmy-Noether-Programme, Projekt
525 nummer 396311425 "DEEP QUANTICAMS". We would also like to thank Schmidt Ocean Foundation and the crew and team members of the Falkor cruise

FK190612 for making the entire expedition and the bubble measurements offshore Oregon a success.

References

- 530 [1] S. Beaubien, C. De Vittor, J. Schneider von Deimling, F. Ziogou, D. McGinnis, The panarea natural co2 seeps: fate and impact of the leaking gas (paco2) (2013).
- [2] J. Greinert, Y. Artemov, V. Egorov, M. De Batist, D. McGinnis, 1300-m-high rising bubbles from mud volcanoes at 2080 m in the black sea: Hydroacoustic characteristics and temporal variability, Earth and Planetary
535 Science Letters 244 (1-2) (2006) 1–15.
- [3] P. Urban, K. Köser, J. Greinert, Processing of multibeam water column image data for automated bubble/seep detection and repeated mapping, Limnology and oceanography: methods 15 (1) (2017) 1–21.
- 540 [4] J. Greinert, B. Nützel, Hydroacoustic experiments to establish a method for the determination of methane bubble fluxes at cold seeps, Geo-Marine Letters 24 (2) (2004) 75–85.
- [5] J. Greinert, Monitoring temporal variability of bubble release at seeps: The hydroacoustic swath system gasquant, Journal of Geophysical Research: Oceans 113 (C7) (2008).
545
- [6] R. Merewether, M. S. Olsson, P. Lonsdale, Acoustically detected hydrocarbon plumes rising from 2-km depths in guaymas basin, gulf of california, Journal of Geophysical Research: Solid Earth 90 (B4) (1985) 3075–3085.
- 550 [7] J. S. Von Deimling, J. Greinert, N. Chapman, W. Rabbel, P. Linke, Acoustic imaging of natural gas seepage in the north sea: Sensing bubbles controlled by variable currents, Limnology and Oceanography: Methods 8 (5) (2010) 155–171.

- [8] M. Veloso, J. Mienert, M. De Batist, J. Greinert, Methane flux estimation of a large seep area offshore svalbard based on visual observations and inverse hydroacoustic modeling, in: EGU General Assembly Conference Abstracts, 2014, p. 13130.
- [9] M. Veloso, J. Greinert, J. Mienert, M. De Batist, A new methodology for quantifying bubble flow rates in deep water using splitbeam echosounders: Examples from the arctic offshore nw-svalbard, *Limnology and Oceanography: methods* 13 (6) (2015) 267–287.
- [10] A. Jordt, C. Zelenka, J. S. Von Deimling, R. Koch, K. Köser, The bubble box: Towards an automated visual sensor for 3d analysis and characterization of marine gas release sites, *Sensors* 15 (12) (2015) 30716–30735.
- [11] K. Thomanek, O. Zielinski, H. Sahling, G. Bohrmann, Automated gas bubble imaging at sea floor—a new method of in situ gas flux quantification, *Ocean Science* 6 (2) (2010) 549–562.
- [12] Y. Bian, F. Dong, H. Wang, Reconstruction of rising bubble with digital image processing method, in: 2011 IEEE International Instrumentation and Measurement Technology Conference, IEEE, 2011, pp. 1–6.
- [13] Y. Bian, F. Dong, W. Zhang, H. Wang, C. Tan, Z. Zhang, 3d reconstruction of single rising bubble in water using digital image processing and characteristic matrix, *Particuology* 11 (2) (2013) 170–183.
- [14] C. Zelenka, Gas bubble shape measurement and analysis, in: German Conference on Pattern Recognition, Springer, 2014, pp. 743–749.
- [15] T. Xue, L. Qu, B. Wu, Matching and 3-d reconstruction of multibubbles based on virtual stereo vision, *IEEE Transactions on Instrumentation and Measurement* 63 (6) (2013) 1639–1647.
- [16] I. Leifer, G. de Leeuw, L. H. Cohen, Optical measurement of bubbles: System design and application, *Journal of Atmospheric and Oceanic Technology* 20 (2003) 1317–1332.

- [17] B. Wang, S. A. Socolofsky, A deep-sea, high-speed, stereoscopic imaging system for in situ measurement of natural seep bubble and droplet characteristics, *Deep Sea Research Part I: Oceanographic Research Papers* 104 (2015) 134–148.
- 585 [18] R. J. Adrian, Particle-imaging techniques for experimental fluid mechanics, *Annual review of fluid mechanics* 23 (1) (1991) 261–304.
- [19] Y. Fu, Y. Liu, Development of a robust image processing technique for bubbly flow measurement in a narrow rectangular channel, *International Journal of Multiphase Flow* 84 (2016) 217–228.
- 590 [20] D. G. Lowe, Distinctive image features from scale-invariant keypoints, *International Journal of Computer Vision* 60 (2) (2004) 91–110.
URL <http://citeseerx.ist.psu.edu/viewdoc/summary?doi=10.1.1.2.8899>
- [21] H. Hirschmuller, Stereo processing by semiglobal matching and mutual in-
595 formation, *IEEE Transactions on pattern analysis and machine intelligence* 30 (2) (2007) 328–341.
- [22] T. Xue, L. Qu, Z. Cao, T. Zhang, Three-dimensional feature parameters measurement of bubbles in gas–liquid two-phase flow based on virtual stereo vision, *Flow Measurement and Instrumentation* 27 (2012) 29–36.
- 600 [23] Y. Fu, Y. Liu, 3d bubble reconstruction using multiple cameras and space carving method, *Measurement Science and Technology* 29 (7) (2018) 075206.
- [24] A. U. M. Masuk, A. Salibindla, R. Ni, A robust virtual-camera 3d shape reconstruction of deforming bubbles/droplets with additional physical con-
605 straints, *International Journal of Multiphase Flow* 120 (2019) 103088.
- [25] H. Sahling, G. Bohrmann, Y. G. Artemov, A. Bahr, M. Brüning, S. A. Klapp, I. Klaucke, E. Kozlova, A. Nikolovska, T. Pape, et al., Vodyanitskii

- mud volcano, sorokin trough, black sea: Geological characterization and quantification of gas bubble streams, *Marine and Petroleum Geology* 26 (9) (2009) 1799–1811.
- [26] B. Wang, S. A. Socolofsky, J. A. Breier, J. S. Seewald, Observations of bubbles in natural seep flares at mc 118 and gc 600 using in situ quantitative imaging, *Journal of Geophysical Research: Oceans* 121 (4) (2016) 2203–2230.
- [27] A. Agrawal, Y. Taguchi, S. Ramalingam, Analytical forward projection for axial non-central dioptric and catadioptric cameras, in: *European Conference on Computer Vision*, Springer, 2010, pp. 129–143.
- [28] A. Jordt-Sedlazeck, R. Koch, Refractive calibration of underwater cameras, in: A. Fitzgibbon, S. Lazebnik, P. Pietro, Y. Sato, C. Schmid (Eds.), *Computer Vision - ECCV 2012*, Vol. 7576 of *Lecture Notes in Computer Science*, Springer Berlin Heidelberg, 2012, pp. 846–859.
- [29] M. She, K. Köser, Considering spherical refraction in visual ocean gas release quantification, in: *2020 International Conference on Computer Vision, Image and Deep Learning (CVIDL)*, IEEE, 2020, pp. 64–69.
- [30] M. She, Y. Song, J. Mohrmann, K. Köser, Adjustment and calibration of dome port camera systems for underwater vision, in: *German Conference on Pattern Recognition*, Springer, 2019, pp. 79–92.
- [31] M. She, D. Nakath, Y. Song, K. Köser, Refractive geometry for underwater domes, *ISPRS Journal of Photogrammetry and Remote Sensing* 183 (2022) 525–540.
- [32] I. Leifer, R. K. Patro, The bubble mechanism for methane transport from the shallow sea bed to the surface: A review and sensitivity study, *Continental Shelf Research* 22 (16) (2002) 2409–2428.
- [33] Z. Zhang, A flexible new technique for camera calibration, *IEEE Transactions on pattern analysis and machine intelligence* 22 (2000).

- [34] R. Hartley, A. Zisserman, Multiple View Geometry in Computer Vision (Second Edition), 2nd Edition, Cambridge University Press, 2004.
- [35] L. Leal-Taixé, A. Milan, K. Schindler, D. Cremers, I. Reid, S. Roth, Tracking the trackers: an analysis of the state of the art in multiple object tracking, arXiv preprint arXiv:1704.02781 (2017).
640
- [36] A. Bewley, Z. Ge, L. Ott, F. Ramos, B. Upcroft, Simple online and real-time tracking, in: 2016 IEEE international conference on image processing (ICIP), IEEE, 2016, pp. 3464–3468.
- [37] M. Mario E. Veloso-Alarcón, J. Greinert, P. Urban, T. W. Weiss, K. Köser, Optical and hydroacoustical monitoring of methane seep sites offshore Oregon, in review.
645